

Numerical assessment of coaptation for auto-pericardium based aortic valve cusps

V. Yu. Salamatova^{*†}, A. A. Liogky^{*}, P. A. Karavaikin^{†‡}, A. A. Danilov^{§*†},
P. Y. Kopylov[†], G. V. Kopytov[¶], O. N. Kosukhin^{||†}, R. A. Pryamonosov[†],
A. A. Shipilov^{**†}, A. S. Yurova[†], and Yu. V. Vassilevski^{*†§||}

Abstract — Aortic valve disease accounts for 45% of deaths from heart valve diseases. An appealing approach to treat aortic valve disease is surgical replacement of the valve leaflets based on chemically treated autologous pericardium. This procedure is attractive due to its low cost and high effectiveness. We aim to develop a computational technology for patient-specific assessment of reconstructed aortic valve function that can be used by surgeons at the preoperative stage. The framework includes automatic computer tomography image segmentation, mesh generation, simulation of valve leaflet deformation. The final decision will be based on uncertainty analysis and leaflet shape optimization. This paper gives a proof of concept of our methodology: simulation methods are presented and studied numerically.

Keywords: Aortic valve, mass–spring model, hyperelastic nodal force

MSC 2010: 92C10, 74G15

Due to increase in life expectancy in high-income countries, heart valve disease is now referred as the ‘next cardiac epidemic’ [3]. Aortic valve disease (AVD) accounts for 45% of deaths from heart valve disease [3]. An appealing approach to treat AVD is surgical replacement of the valve leaflets based on chemically treated autologous pericardium. This procedure is attractive due to its low cost and high effectiveness [19]. During the surgical procedure, surgeons excise the patch of the patient pericardium, fix it with glutaraldehyde solution with a buffer for 10 minutes, and construct the new leaflets of the aortic valve. The decision on the new aortic leaflet design is made during the surgical procedure based on surgeon’s experience

^{*}Moscow Institute of Physics and Technology, Dolgoprudny 141701, Russia

[†]Sechenov University, Moscow 119991, Russia. E-mail: salamatova@gmail.com

[‡]Central Clinical Hospital of the Presidential Administration of the Russian Federation, Moscow 121359, Russia

[§]Marchuk Institute of Numerical Mathematics, Russian Academy of Sciences, Moscow 119333, Russia

[¶]Baltic Federal University, Kaliningrad 236038, Russia

^{||}Lomonosov Moscow State University, Moscow 119991, Russia

^{**}Moscow Center of Advanced Sports Technologies, Moscow 129272, Russia

The work was supported by the RFBR grants 18-00-01524, 18-31-20048, 17-01-00886.

and expertise. Success of the operation relies on the valve competence under diastolic pressure in terms of coaptation characteristics. Intra-operative testing of the reconstructed valve in its diastolic state is demanded [2]. A surgical planning system based on patient-specific modelling will allow surgeons to compare different aortic leaflet designs, to choose optimal replacement strategies and to reduce duration of surgery. This preoperative preparation stage in its turn can enhance significantly the surgical outcome.

Model-based optimization of the valve leaflets is very important. Parametric geometric models suggest an ‘ideal valve’ which optimizes coaptation and eliminates regurgitation (see, e.g., [8, 12]) disregarding patient’s geometry, i.e., the features of patient’s anatomy. We aim to develop a computational technology for patient-specific assessment of reconstructed aortic valve function that can be used by surgeons at the preoperative stage. The technological pipeline consists of four stages. The first stage is medical image segmentation providing patient-specific geometry of the aortic root and the aorta. The second stage is choosing trial valve leaflet design based on geometric features of the aortic root. The next stage is simulation of those leaflets closure and estimation of coaptation characteristics under the diastolic pressure. The final stage is optimization of leaflets design and/or size based on computed coaptation quantities. In this article we focus on the first and the third stages of the pipeline, the problem of leaflet design and optimization will be addressed in our future works.

Clinical application of the computational technology implies obtaining of simulation results on-the-fly to be able to test different valve configurations. This imposes specific restrictions on the most time-consuming part of the simulation: modelling of leaflets deformation (valve closure) should be as fast as possible. Most of the studies on the numerical modelling of the aortic valve (AV) do not report simulation times. Computational complexity of a model correlates with its accuracy and detailization. For instance, the fluid-structure interaction (FSI) model, the most realistic computational tool describing AV functionality, is compared in [22] with the corresponding structural finite element model (FEM) in terms of stresses, coaptation, AV dynamics, etc. Two models shared the same aortic root and aortic valve geometry, mechanical properties of the tissue and the kinematic boundary conditions. The AV leaflets and the aorta were discretized by shell and linear elements, respectively, and hybrid Eulerian-Lagrangian approach with penalty-based coupling was used for FSI modelling. Dynamic simulations of one cardiac cycle were performed on workstation with 12 processors by the commercial finite element solver LS-DYNA. Although only the FSI model recovers AV transient motion and blood dynamics, AV diastolic coaptation characteristics in terms of level and length were almost the same in the structural and FSI models (the difference was 0.1 mm). Simulations required 185 hours and 19 hours for the FSI model and structural FEM, respectively. Computational complexity of structural FE modelling of the mitral valve is reported in [25] for one closing cycle (13 hours on 16 processors) and in [18] for systolic mitral valve closure (73–98 min on 16 processors). Although FE simulation of valve closure is much faster than that of the whole cardiac cycle, the computa-

tional time is still prohibitively high for the use in real-time patient-specific surgical planning. The reasons for high complexity of FE simulations of the heart valves are large deformations, complex constitutive relations, and high numerical stiffness of the involved equations.

For real-time surgical planning system the method of modelling aortic valve closure in its diastolic state should be computationally cheap and should provide the results within a few minutes on a personal computer. In the present study we consider and compare two efficient methods for computation of the AV closure. The first approach is the very popular in computer graphics Mass-spring model (MSM) [23]. MSM represents the deformable body by a set of point masses interconnected by elastic springs. Although stresses can not be recovered by MSM, in some cases large deformations may be recovered satisfactorily. In particular, comparisons of the MSM- and FEM-based predictions of the coaptation zone of the closed heart valve [10, 11, 18] demonstrate feasibility and efficiency of MSM. The second approach is based on the hyperelastic nodal force method [21, 24], which is a generalization of the triangular biquadratic springs method proposed in [5] for St-Venant-Kirchhoff isotropic hyperelastic membranes. The method [5] establishes a formal connection between FEM and MSM based on the variational principle and interpolation properties of barycentric coordinates. The hyperelastic nodal force method [21, 24] expands the method [5] for other hyperelastic materials and obtains easy-to-implement concise formulas for nodal elastic forces sacrificing corresponding springs representation. In the scope of our study, we consider membrane formulations (no resistance to bending loads) applicable to simulation of the AV diastolic state since ‘the leaflets are operating in the regime, where in-plane stresses are relatively large, at least an order of magnitude greater than bending stresses’ [10].

Patient-specific modelling implies personalized aorta geometry and material models. We use an elaborated algorithm of medical image segmentation to retrieve the patient’s aorta geometry. As the patient-specific pericardium material property is unknown, in order to estimate the impact of material parameters and material models on coaptation characteristics, we carry out the sensitivity analysis. Besides the first application of the hyperelastic nodal force method, the novelty of the study is experimental discovery that the coaptation profile is almost invariant to a type of isotropic hyperelastic material and depends only on the elastic modulus, whereas the coaptation heights are sensitive to both material model and elastic modulus.

The outline of the paper is as follows. In Section 1 we describe the techniques for the geometric representation of the aortic valve. The efficient methods of modelling valve closure are described in Section 2. The results of numerical experiments are presented in Section 3.

1. Geometry of the aortic valve and its leaflets

A conventional image of contrast enhanced Computer Tomography Angiography (ceCTA) is processed at the first stage of our computational technology. At this stage we reconstruct the boundaries of the patient’s aortic root and detect the com-

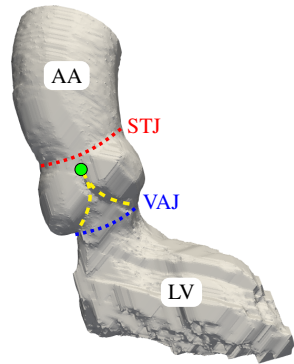


Figure 1. Segmented boundaries of aortic root and part of left ventricle: ascending aorta (AA), sinotubular junction (STJ), commissure point (green dot), suturing path (yellow dashed line), ventriculo-aortic junction (VAJ), part of the left ventricle (LV), aortic sinuses are between suturing path and sinotubular junction.

missure points where the valve leaflets meet each other. Since we are interested in assessment of the reconstructed valve with the new leaflets, we need only the aortic root geometry. Positions of the future commissure points and suturing paths are assigned by the surgeon.

The aorta segmentation algorithm [4] is based on the Hough Circleness filter [6], the Isoperimetric Distance Trees (IDT) algorithm [7], and mathematical morphology operations. The Hough Circleness filter detects the biggest bright circle on the topmost 2D slice of the image and assign it to the cross-section of the ascending aorta. The center of that bright circle is the seed for the region growth by a high-pass thresholding procedure. It results in an initial mask M_i containing the aorta, the left ventricle and other bright parts of the ceCTA image. Mask M_i is processed further by the IDT algorithm and mathematical morphology operations to produce a mask M_a for the aorta and a top part of the left ventricle (see [4]). Having on input mask M_a , ITK SNAP software [26] and CGAL library [20] generate a surface mesh by the marching cubes algorithm. The surface mesh includes the boundaries of the ascending aorta, the sinotubular junction, the aortic sinuses, the ventriculo-aortic junction, and a part of the left ventricle (see Fig. 1). The surface mesh is used for visualization of the patient-specific domain and manual assignment of the suturing path for the replaced leaflets.

The leaflet shape optimization procedure assumes that the shape is defined by a parameterized template. In this work we use a tentative flat shape design shown in Fig. 2. The symmetric shape of the template is based on the shape recommended by Dr. S.Ozaki [17]. The boundary has a circular arc ($B - C$) at the bottom extended by straight tangent segments ($B - A$ and $C - D$). The top part of the leaflet ($A - E - D$) represents the free boundary. The following parameters define a leaflet uniquely: the radius of circular arc r , the circular arc angle $\angle BOC$ α (in this paper it is fixed, $\alpha = 160^\circ$), the length of extension segments ($B - A$ and $C - D$) a , the length of free segments ($A - E$ and $E - D$) b .

The total length of the sutured edge is equal to $2a + \pi r \alpha / 180$, the total length

forces are applied:

$$\mathbf{F}_i^{\text{res}} \equiv \mathbf{F}_i^p + \mathbf{F}_i^e + \mathbf{F}_i^c = 0 \quad (2.1)$$

where \mathbf{F}_i^p , \mathbf{F}_i^e , and \mathbf{F}_i^c are the force of blood pressure, the elastic force, and the contact force from other leaflets, respectively.

To find the static equilibrium, we apply the iterative process described by Algorithm 2.1. Here $G^n(\mathbf{r}_1^n, \dots, \mathbf{r}_N^n)$ is the oriented triangulated surface with N nodes and M triangles at the n th iteration, \mathbf{r}_i^n is the position of the i th node at the n th iteration, $\Delta\mathbf{r}_i^n$ is the shift of the i th node applied at the n th iteration, $\mathbf{F}_i^{\text{res}}(G^n)$ is the resulting force applied to the i th node at the current state of G^n , δ is a small coefficient converting the total force into the shift. The iterations terminate when $\|\Delta\mathbf{r}^n\| < 10^{-3}\|\Delta\mathbf{r}^0\|$.

Algorithm 2.1

Require: mesh $G^0(\mathbf{r}_1^0, \dots, \mathbf{r}_N^0)$

- 1: **for** $i = 1, \dots, N$ **do** ▷ initialization
 - 2: set \mathbf{r}_i^0 as initial position of the i th node
 - 3: **end for**
 - 4: set pressure P , const δ , $n = 0$
 - 5: **repeat** ▷ iteration
 - 6: **for** $i = 1, \dots, N$ **do**
 - 7: compute total force $\mathbf{F}_i^{\text{res}} \leftarrow \mathbf{F}_i^{\text{res}}(G^n)$
 - 8: $\Delta\mathbf{r}_i^n = \delta \cdot \mathbf{F}_i^{\text{res}}$
 - 9: $\mathbf{r}_i^{n+1} = \mathbf{r}_i^n + \Delta\mathbf{r}_i^n$
 - 10: **end for**
 - 11: update mesh surface $G^{n+1}(\mathbf{r}_1^{n+1}, \dots, \mathbf{r}_N^{n+1})$
 - 12: $n \leftarrow n + 1$
 - 13: **until** the process has converged
-

The pressure force \mathbf{F}_i^p is defined by $\mathbf{F}_i^p = P \sum_T A_T \mathbf{n}_T / 3$, where P is the applied pressure, \mathbf{n}_T is the unit normal to triangle T with area A_T , $\sum_T A_T \mathbf{n}_T$ is the sum of areas of all oriented triangles T sharing the i th node.

The leaflets can not interpenetrate, they interact with each other forming a coaptation zone to be evaluated. The coaptation zone, the coaptation profile, and other basic notions for one leaflet are schematically represented in Fig. 4. To describe the contact interaction, we introduce the *contact forces* which are similar to the reaction forces [18]. To this end, for each surface triangle T with vertices $\mathbf{r}_i, \mathbf{r}_j, \mathbf{r}_k$, and the external unit normal \mathbf{n}_T we define its barycenter as $\mathbf{r}_T = (\mathbf{r}_i + \mathbf{r}_j + \mathbf{r}_k) / 3$, and for the current mesh G we define the threshold

$$d = 1.1M^{-1} \sum_{T \in G} \max(\|\mathbf{r}_T - \mathbf{r}_i\|, \|\mathbf{r}_T - \mathbf{r}_j\|, \|\mathbf{r}_T - \mathbf{r}_k\|).$$

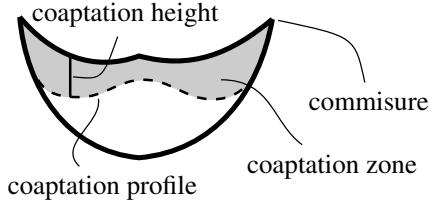


Figure 4. Characteristics of the coaptation zone.

For each grid node \mathbf{r}_i from the d -vicinity of triangle T (i.e., $\|\mathbf{r}_i - \mathbf{r}_T\| < d$) we compute the new tentative position $\tilde{\mathbf{r}}_i$ neglecting the contact forces from the other leaflets. We also compute the signed distance to the plane of the triangle $d_{i,T}^\pi = (\tilde{\mathbf{r}}_i - \mathbf{r}_T, \mathbf{n}_T)$. If the signed distance $d_{i,T}^\pi$ is below the threshold $d^\pi = 0.7$ mm, then we apply the contact force

$$\mathbf{F}_{i,T}^c = \begin{cases} \|\mathbf{F}_i\| \exp\left(-\frac{k_1 d_{i,T}^\pi}{\|\mathbf{F}_i\|}\right) \mathbf{n}_T, & d_{i,T}^\pi > 0 \\ (\|\mathbf{F}_i\| - k_2 d_{i,T}^\pi) \mathbf{n}_T, & d_{i,T}^\pi \leq 0 \end{cases} \quad (2.2)$$

where $\mathbf{F}_i = \mathbf{F}_i^p + \mathbf{F}_i^e$, and $k_1 = 0.8$ N/m and $k_2 = 20$ N/m are the empirically selected constants. The total contact force at the node of the leaflet grid is the sum of all contact forces from surrounding triangles forming the other leaflets.

We still need to define the nodal elastic force \mathbf{F}_i^e . We use two methods for computation of \mathbf{F}_i^e .

The first method is based on the simple mass–spring model (MSM) [23]: $\mathbf{F}_i^s = \sum_{e_{ij}} \mathbf{F}_{ij}$, where the summation is taken over all mesh edges e_{ij} incident to the mesh node i . The elastic force \mathbf{F}_{ij} of a virtual spring connecting the i th and j th nodes depends on the spring deformation:

$$\mathbf{F}_{ij} = k_{ij}(\|\mathbf{r}_j - \mathbf{r}_i\| - L_{ij}) \frac{\mathbf{r}_j - \mathbf{r}_i}{\|\mathbf{r}_j - \mathbf{r}_i\|}, \quad k_{ij} = \frac{E(\varepsilon, \alpha_0) H A_{ij}}{L_{ij}^2} \quad (2.3)$$

where H is the average surface thickness, A_{ij} is the surface area of the two triangles sharing the edge e_{ij} of length L_{ij} , A_{ij} and L_{ij} are computed on the flat undeformed grid, $E = E(\varepsilon, \alpha_0)$ is the elastic modulus of the leaflet tissue depending on the strain ε and structural characteristics α_0 . An example of $E(\varepsilon, \alpha_0)$ for a nonlinear anisotropic material is given in [10]:

$$E(\varepsilon, \alpha_0) = \sqrt{E_f^2(\varepsilon) \sin^2 \alpha_0 + E_{cf}^2(\varepsilon) \cos^2 \alpha_0} \quad (2.4)$$

where $E_f(\varepsilon)$ and $E_{cf}(\varepsilon)$ are the parameters based on the experimental stress–strain curves in the fiber and cross-fiber direction, respectively, ε is the relative elongation of the spring, α_0 is the angle between the spring initial orientation and a preferential direction of the collagen fibers within the leaflet tissue.

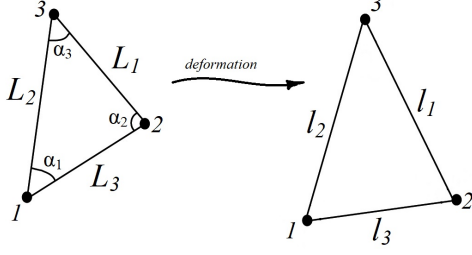


Figure 5. Triangle before and after deformation.

The second method is the hyperelastic nodal force (HNF) method suggested in [21, 24]. It defines the elastic nodal force for arbitrary (isotropic or anisotropic) hyperelastic material with given elastic potential U . We assume that each triangle T of the undeformed flat grid with area A_T , edge lengths L_m and angles α_m , $m = 1, 2, 3$ (see Fig.5), is mapped by the leaflet deformation to a triangle T' with vertices $\mathbf{r}_i, \mathbf{r}_j, \mathbf{r}_k$ and edge lengths l_m and that the discretized counterpart $U_d(\mathbf{r}_i, \mathbf{r}_j, \mathbf{r}_k)$ of the elastic potential U is known. Then the hyperelastic nodal force is

$$\mathbf{F}_i^e(T) = -A_T \frac{\partial U_d(\mathbf{r}_i, \mathbf{r}_j, \mathbf{r}_k)}{\partial \mathbf{r}_i}. \quad (2.5)$$

For general elastic potentials given in terms of invariants of the right Cauchy–Green tensor, the authors of [21, 24] derived easy-to-implement concise formulas for nodal elastic forces (2.5).

In particular case of an isotropic hyperelastic St.Venant–Kirchhoff membrane, the hyperelastic nodal force is computed as the sum of reactions of deformed triangular biquadratic springs (TBS) [5]:

$$\begin{aligned} \mathbf{F}_i^e(T) &= \sum_{j \neq i} \varkappa_k^T \Delta^2 l_k (\mathbf{r}_j - \mathbf{r}_i) + \sum_{j \neq i} (c_j^T \Delta^2 l_i + c_i^T \Delta^2 l_j) (\mathbf{r}_j - \mathbf{r}_i) \\ \Delta^2 l_i &= l_i^2 - L_i^2 = \|\mathbf{r}_j - \mathbf{r}_k\|^2 - L_i^2 \\ \varkappa_k^T &= \frac{2 \cot^2 \alpha_k (\lambda + \mu) + \mu}{16 A_T} = \frac{E(2 \cot^2 \alpha_k + 1 - \nu)}{16(1 - \nu^2) A_T} \\ c_k^T &= \frac{2 \cot \alpha_i \cot \alpha_j (\lambda + \mu) - \mu}{16 A_T} = \frac{E(2 \cot \alpha_i \cot \alpha_j + \nu - 1)}{16(1 - \nu^2) A_T} \end{aligned} \quad (2.6)$$

where λ and μ are Lamé coefficients, E is Young's modulus, ν is Poisson's coefficient, indices i, j, k form the even permutation, stiffnesses of springs \varkappa_k^T and c_k^T are defined with respect to the undeformed geometry. It is worth noting that the TBS forces are applicable to 2D isotropic St.Venant–Kirchhoff material only, whereas the hyperelastic nodal forces are applicable to any 2D or 3D hyperelastic material (isotropic or anisotropic).



Figure 6. Three closed cusps in benchmark problem proposed in [16] (a); the coaptation area of the leaflet and its profile (b).

3. Numerical results

We present verification of the numerical models for an aortic valve closure benchmark and their sensitivity study for a real anatomy geometry. All our simulations were run on a laptop Intel Core with i5-8250U CPU 1.60 GHz.

3.1. Aortic valve closure benchmark

We verify the mass-spring model (MSM), the triangular biquadratic spring (TBS) method and the hyperelastic nodal force (HNF) method by the benchmark problem [16]. We consider an aortic healthy valve with aortic annulus (AA) diameter $d_{AA} = 24$ mm and three symmetric leaflets with thickness $H = 0.3$ mm shown in Fig. 6a (it corresponds to the base geometry, Fig. 1 in [16]). Four coaptation characteristics are calculated in [16]: h_E , h_{C-C} , h_{avr} , and NCCA. The effective height h_E is defined as the valve height of the closed valve at pressure load of 3 mm Hg. The value h_{C-C} is the coaptation height measured in the $C-C$ plane which is orthogonal to one of the coaptation planes, is parallel to the AA axis and is distanced from the AA axis by 5 mm. The average coaptation height h_{avr} is defined as the ratio of the coaptation area (bounded by the yellow-red curve in Fig. 6b) and the free-edge length (the red curve in Fig. 6b) under the diastolic pressure of 80 mm Hg. The normalized cusp coaptation area NCCA is defined as the ratio of the coaptation area and the total cusp surface area (bounded by the green-red curve in Fig. 6b). The h_E was calculated in [16] from so-called dry static models ignoring the blood flow, the other parameters were calculated from a general fluid-structure interaction (FSI) model. The material of the leaflets is assumed in [16] to be linear elastic with $E = 1$ MPa and $\nu = 0.45$.

We compare the coaptation characteristics computed by MSM (linear elastic material with $E = 1$ MPa, $\nu = 0.45$), TBS method (St.Venant–Kirchhoff material with $E = 1$ MPa, $\nu = 0.45$), HNF method (incompressible neo-Hookean material with $E = 1$ MPa, $\mu = E/3$ and incompressible Gent material with $E = 1$ MPa, $\mu = E/3$, $J_m = 2.3$). For the last two materials the elastic potentials are

$$U_{NH} = H\mu/2(I_1 + 1/I_2 - 3) \quad (3.1)$$

$$U_{Gent} = -HJ_m\mu/2\ln(1 - (I_1 + 1/I_2 - 3)/J_m) \quad (3.2)$$

Table 1. Comparison of the coaptation heights h_E , h_{C-C} , h_{avr} and normalized cusp coaptation area NCCA.

Model	h_E , mm	h_{C-C} , mm	h_{avr} , mm	NCCA, %	CPU time, sec
FSI, lin.elasticity [16]	10.5	1.5	2.7	21	n/a
MSM (2.3)	10.8	3.8	3.3	25	44
TBS (2.6)	10.8	3.1	2.9	24	58
neo-Hookean (2.5)–(3.1)	10.4	3.0	2.5	21	136
Gent (2.5)–(3.2)	10.8	3.4	3.1	24	203

where I_1 and I_2 are 2D strain invariants, H is the thickness before the deformation, μ is the shear modulus, J_m is a material constant.

Table 2. Elastic moduli derived from experimental data for treated human pericardium [27] ($\lambda_1^* = 0.175$, $\lambda_2^* = 0.3$).

	E_1 (kPa)	E_2 (kPa)	E_3 (kPa)
Longitudinal direction (E_f)	137	568	968
Transverse direction (E_{cf})	63	570	1400
Average isotropic case	106	569	1200

Table 3. MSM-based values of the coaptation heights h and h_c (mm) for three templates and three anisotropy directions (\uparrow , \rightarrow , \nearrow are cases of vertical, horizontal and diagonal direction of anisotropy, respectively).

Leaflet template		Isotropic	\uparrow	\rightarrow	\nearrow
a	h	14.3	14.3	14.2	14.2
b	h	16.4	16.2	16.3	16.6
c	h	16.8	16.2	17.0	16.9
a	h_c	0	0	0	0
b	h_c	11.6	10	10.1	12.2
c	h_c	11.9	13.4	12.7	13.2

Table 4. Sensitivity of MSM-based coaptation heights h and h_c to elastic moduli E_1 and E_2 .

E_1 (kPa)	E_2 (kPa)	h (mm)	h_c (mm)
50	300	18.4	13.6
50	569	17.2	10.9
106	300	17.3	12.9
106	569	16.4	11.6
106	700	15.7	11.6
180	569	15.6	9.7
180	700	15.4	9.2

The obtained coaptation characteristics are given in Table 1. The grid for each leaflet contains 1313 triangles. Further mesh refinement does not change the results except for the TBS model where $h_E = 11$ mm, $h_{C-C} = 3.6$ mm, $h_{avr} = 3.5$ mm, NCCA= 28% on the mesh with halved mesh size. This implies slower mesh convergence of the TBS scheme compared to the other methods. The FSI-based value of h_{C-C} is less than h_{C-C} from our structural simulations, although profiles of the coaptation area (see Fig. 6b) are similar to the profile presented in Fig. 4 [16]. In the literature, the comparison of the coaptation characteristics for FSI-based models and dry static models is controversial: in [15] dry models overestimate the coapta-

Table 5. Sensitivity of coaptation heights h , h_c , and h_{C-C} to elasticity model and values of elastic moduli.

Model		h , mm	h_c , mm	h_{C-C} , mm	CPU time, sec
MSM	$E = 10$ MPa	15.4	7.3	13.1	282
TBS	$E = 10$ MPa, $\nu = 0.5$	15.4	8.3	15.1	578
Neo-Hookean	$E = 10$ MPa, $\mu = E/3$	13.0	7.3	12.9	527
Gent	$E = 10$ MPa, $\mu = E/3$, $J_m = 2.3$	15.5	8.4	13.5	2072
MSM	$E = 1$ MPa	17.3	10.7	16.0	143
TBS	$E = 1$ MPa, $\nu = 0.5$	16.7	12.1	16.2	426
Neo-Hookean	$E = 1$ MPa, $\mu = E/3$	17.4	8.2	15.8	464
Gent	$E = 1$ MPa, $\mu = E/3$, $J_m = 2.3$	16.3	10.5	15.9	2612
MSM	$E = 0.1$ MPa	21.5	19.6	20.3	166
TBS	$E = 0.1$ MPa, $\nu = 0.5$	23.7	19.7	23.4	191
Gent	$E = 0.1$ MPa, $\mu = E/3$, $J_m = 2.3$	23.6	19.0	23.2	546

tion heights, whereas in [22] they are almost the same. The discrepancy stems from different boundary conditions (see [22, Sect. 4.1]).

In general, the coaptation heights due to the dry static models deviate by no more than 2 mm, they match h_E , h_{avt} from [16] within 0.6 mm tolerance and overestimate h_{C-C} from [16] by 1.5–2.3 mm.

3.2. Sensitivity analysis on realistic geometric data

Here we consider the case of patient-specific geometry based on the ceCTA data of a real patient. We examine leaflet templates presented in Fig. 3. In our simulation we calculate under the diastolic pressure 80 mmHg the maximal coaptation height h and the central coaptation height h_c defined in Fig. 7a. These coaptation characteristics are thought to be the main geometric criteria for further optimization of leaflet designs.

To be as close as possible to the clinical application, we assume that the leaflets are cut from the treated human pericardium. There is no consensus on mechanical properties of fresh and treated human pericardium. According to the review [1], human pericardium is isotropic (both fresh and treated) whereas animal pericardium is anisotropic. However, according to the experimental work [27], the human pericardium is anisotropic (both fresh and treated). For this reason we estimate the influence of anisotropy using the mass–spring model and the stress–strain data approximated by function [27]:

$$E(\varepsilon) = \begin{cases} E_1, & \varepsilon \leq \lambda_1^* \\ E_2, & \lambda_1^* < \varepsilon < \lambda_2^* \\ E_3, & \varepsilon \geq \lambda_2^* \end{cases} \quad (3.3)$$

with parameters defined in Table 2 and strain ε represented by the relative elongation. We use equation (2.4) to calculate the elastic moduli and consider different directions of anisotropy represented by fibers orientation. The calculated coaptation



Figure 7. Definitions of the coaptation zone, maximal coaptation height h and the central coaptation height h_c (a); position of leaflets inside the aorta (b).

heights are presented in Table 3. Each triangulated leaflet has about 400 elements. Thickness of the pericardium H is equal to 0.3 mm. An example of the computed coaptation zone is shown in Fig. 7b. The maximal coaptation height h does not depend on anisotropy direction whereas the central height h_c is slightly sensitive to the anisotropy.

To study the sensitivity of the coaptation heights to the material parameters, we vary elastic moduli in the range recovered for 44 patients [27]. We consider the mass-spring model and the template (b) shown in Fig. 3. The material is considered to be isotropic with the stress–strain relationship (3.3) where $E_3 = 1200$ kPa, $\lambda_1^* = 0.175$, $\lambda_2^* = 0.3$. The impact of the elastic moduli E_1 and E_2 on the coaptation heights is essential, the deviations may achieve 4 mm (see Table 4).

We also study the influence of the material model on the coaptation heights h , h_c , h_{C-C} . We consider MSM, TBS, neo-Hookean, Gent models with different elastic moduli, $E = 10^5, 10^6, 10^7$ Pa. The coaptation heights are shown in Table 5 and the coaptation profiles are shown in Fig. 8a. The coaptation profile here is the boundary of the coaptation zone projected to the undeformed flat triangulation. The profiles are non-symmetric since the aortic annulus is non-symmetric (see Fig. 8b). Surprisingly, the coaptation profiles are not sensitive to the material model but depend on the elastic modulus E . However, the variations of h , h_c , h_{C-C} among different models with the same elastic modulus E are considerable since the deformation of cusps is model-sensitive. For different elastic moduli or elastic models the variations in the coaptation heights may reach 3–10 mm (rf. Tables 4 and 5).

4. Conclusions

We presented the numerical framework for computing the coaptation characteristics of the reconstructed aortic valve. We analyzed different approaches for modelling of the AV closure. The approaches are appealing in clinical applications since they require only a few minutes of computations on a laptop. The coaptation zone is the main factor for decision making in leaflet shape optimization. The shape optimization targets the coaptation zone only, and we address the static equilibrium of the closed reconstructed valve under the diastolic pressure. Our numerical results for

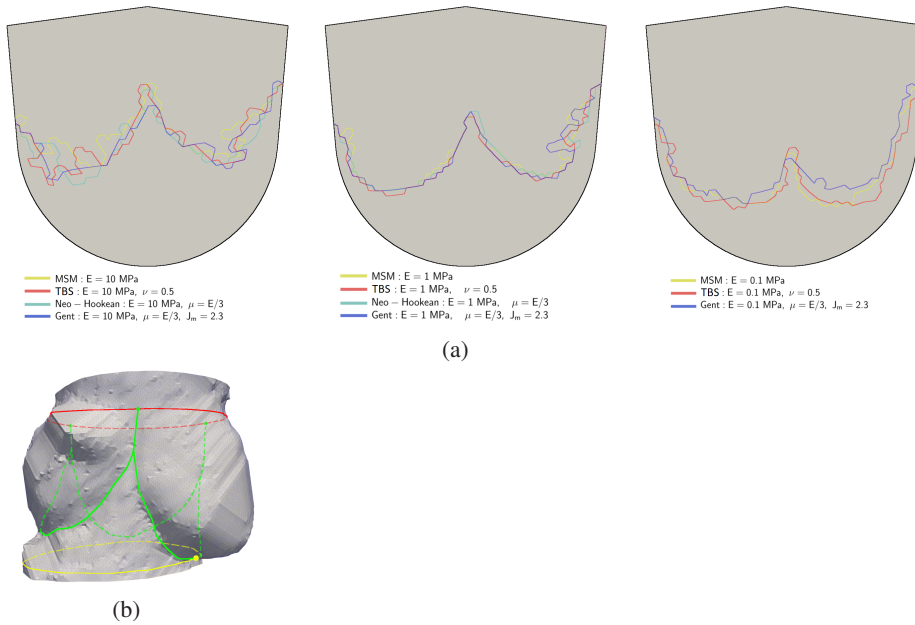


Figure 8. Coaptation profiles for different elasticity models and elastic moduli (a), suturing paths and commissures on the aorta (b).

the coaptation zone are in good agreement with the benchmark problem [16]. To develop the computational patient-specific aortic valve reconstruction, we elaborated the algorithm for automatic aorta segmentation and meshing and carried out elastic models sensitivity analysis within the range of human pericardium mechanical properties [27]. We found that the coaptation profile is insensitive to the elasticity models with the same elastic modulus. However, the variations of the coaptation heights may achieve 3–10 mm for different moduli and models. This is large variation since the coaptation heights must be at least 3–4 mm to avoid regurgitation (backward blood flow). The sensitivity to anisotropy of the pericardium was assessed for the mass-spring model: the variations of the heights are about 1 mm that is not essential for the application.

The practical outcome of our research is the conclusion that optimization of the coaptation profile on the leaflet does not require the model specification, only the geometry and the elastic modulus matter. On the other hand, optimization of the coaptation heights requires specification of the pericardium elastic model.

In our future work, we plan to compare our numerical model with real surgical cases of valve reconstruction and obtain more experimental data on mechanical data for fresh and treated pericardium.

References

1. P. Aguiari, M. Fiorese, L. Iop, G. Gerosa, and A. Bagno, Mechanical testing of pericardium for manufacturing prosthetic heart valves. *Interactive Cardiovascular and Thoracic Surgery* **22**

- (2015), No. 1, 72–84.
2. I. G. Berra, P. E. Hammer, S. Berra, A. O. Irusta, S. C. Ryu, D. P. Perrin, N. V. Vasilyev, C. J. Cornelis, P. G. Delucis, and J. Pedro. An intraoperative test device for aortic valve repair. *J. Thoracic and cardiovascular surgery* **157** (2019), No. 1, 126–132.
 3. S. Coffey, B. J. Cairns, and B. Lung, The modern epidemiology of heart valve disease. *Heart* **102** (2016), No. 1, 75–85.
 4. A. Danilov, Yu. Ivanov, R. Pryamonosov, and Yu. Vassilevski, Methods of graph network reconstruction in personalized medicine. *Int. J. Numer. Method. Biomed. Engrg.* (2016), e02754.
 5. H. Delingette, Triangular springs for modeling nonlinear membranes. *IEEE Trans Vis Comput Graph.* **14** (2008), No. 2, 329–341.
 6. R. O. Duda and P. E. Hart, Use of the Hough transformation to detect lines and curves in pictures. *Commun. ACM* **15** (1972), No. 1, 11–15.
 7. L. Grady, Fast, Quality, Segmentation of large volumes—iso-perimetric distance trees. In: *Computer Vision—ECCV 2006. Springer LNCS*, Vol. 3953, 2006, pp. 449–462.
 8. R. Haj-Ali, G. Marom, S. B. Zekry, M. Rosenfeld, and E. Raanani. A general three-dimensional parametric geometry of the native aortic valve and root for biomechanical modeling. *J. Biomechanics* **45** (2012), No. 14, 2392–2397.
 9. P. E. Hammer, D. P. Perrin, J. Pedro, and R. D. Howe, Image-based mass-spring model of mitral valve closure for surgical planning. In: *Proc. of SPIE Medical Imaging: Visualization, Image-guided Procedures, and Modeling* Vol. 6918, 2008, 69180Q.
 10. P. E. Hammer, M. S. Sacks, J. Pedro, and R. D. Howe, Mass-spring model for simulation of heart valve tissue mechanical behavior. *Ann. Biomed. Engrg.* **39** (2011), No. 6, 1668–1679.
 11. P. E. Hammer, J. Pedro, and R. D. Howe, Anisotropic mass-spring method accurately simulates mitral valve closure from image-based models. In: *International Conference on Functional Imaging and Modeling of the Heart* Springer, Berlin, Heidelberg (2011), pp. 233–240.
 12. M. R. Labrosse, C. J. Beller, F. Robicsek, and M. J. Thubrikar, Geometric modeling of functional trileaflet aortic valves: development and clinical applications. *J. Biomechanics* **39** (2006), No. 14, 2665–2672.
 13. K. Lipnikov, Yu. Vassilevski, A. Danilov et al, *Advanced Numerical Instruments 2D*. <https://sourceforge.net/projects/ani2d>
 14. J. Lu, X. Zhou, and M. L. Raghavan, Inverse method of stress analysis for cerebral aneurysms. *Biomechanics and Modeling in Mechanobiology* **7** (2008), No. 6, 477–486.
 15. G. Marom, R. Haj-Ali, E. Raanani, H. J. Schäfers, and M. Rosenfeld, A fluid-structure interaction model of the aortic valve with coaptation and compliant aortic root. *Medical & Biological Engrg. & Computing* **50** (2012), No. 2, 173–182.
 16. G. Marom, R. Haj-Ali, M. Rosenfeld, H. J. Schäfers, and E. Raanani, Aortic root numeric model: Annulus diameter prediction of effective height and coaptation in post-aortic valve repair. *J. Thorac. Cardiovasc. Surg.* **145** (2013), No. 2, 406–411.
 17. S. Ozaki, I. Kawase, H. Yamashita, S. Uchida, Y. Nozawa, M. Takatoh, and S. Hagiwara, A total of 404 cases of aortic valve reconstruction with glutaraldehyde-treated autologous pericardium. *J. Thorac. Cardiovasc. Surg.* **147** (2014), No. 1, 301–306.
 18. O. A. Pappalardo, F. Sturla, F. Onorati, G. Puppini, M. Selmi, G. B. Luciani, G. Faggian, A. Redaelli, and E. Votta, Mass-spring models for the simulation of mitral valve function: Looking for a trade-off between reliability and time-efficiency. *Med. Eng. Phys.* **47** (2017), 93–104.
 19. J. S. Rankin, C. Nöbauer, P. S. Crooke, C. Schreiber, R. Lange, and D. Mazzitelli, Techniques of autologous pericardial leaflet replacement for aortic valve reconstruction. *Ann. Thorac. Surg.* **98**

-
- (2014), No. 2, 743–745.
20. L. Rineau and M. Yvinec, A generic software design for Delaunay refinement meshing. *Computational Geometry* **38** (2007) No. 1-2, 100–110.
 21. V. Yu. Salamatova, Finite element method for 3D deformation of hyperelastic materials. *Diff. Equations* **55** (2019), No. 7, 990-999.
 22. F. Sturla, E. Votta, M. Stevanella, C. A. Conti, and A. Redaelli, Impact of modeling fluid-structure interaction in the computational analysis of aortic root biomechanics. *Medical Engrg.&Physics* **35** (2013), No. 12, 1721–1730.
 23. A. Van Gelder, Approximate simulation of elastic membranes by triangulated spring meshes. *J. Graph. Tools* (1998), No. 3, 21–42.
 24. Yu. V. Vassilevski, V. Yu. Salamatova, and A. V. Lozovskiy, Concise formulas for strain analysis of soft biological tissues. *Diff. Equations* **53** (2017), No. 7, 908–915.
 25. E. Votta, A. Arnoldi, A. Invernizzi, R. Ponzini, F. Veronesi, G. Tamborini, M. Pepi, F. Alamanni, A. Redaelli, and E. G. Caiani, Mitral valve patient-specific finite element modeling from 3D real time echocardiography: a potential new tool for surgical planning. In: *MICCAI Workshop on Cardiovascular Interventional Imaging and Biophysical Modelling*, 2009, 9 p.
 26. P. A. Yushkevich, J. Piven, H. Cody Hazlett, R. Gimpel Smith, S. Ho, J. C. Gee, and G. Gerig, User-guided 3D active contour segmentation of anatomical structures: significantly improved efficiency and reliability. *Neuroimage* **31** (2006), No. 3, 1116–1128.
 27. T. C. Zigras, Biomechanics of Human Pericardium: A Comparative Study of Fresh and Fixed Tissue. *PhD Thesis*, McGill University, 2017.